Simultaneous Readout of Noncommuting Collective Spin Observables beyond the Standard Quantum Limit

Philipp Kunkel, Maximilian Prüfer, Stefan Lannig, Rodrigo Rosa-Medina, Alexis Bonnin, Martin Gärttner, Helmut Strobel, and Markus K. Oberthaler

Kirchhoff-Institut für Physik, Universität Heidelberg, Im Neuenheimer Feld 227, 69120 Heidelberg, Germany

(Received 1 April 2019; published 7 August 2019)

We augment the information extractable from a single absorption image of a spinor Bose-Einstein condensate by coupling to initially empty auxiliary hyperfine states. Performing unitary transformations in both the original and auxiliary hyperfine manifold enables the simultaneous measurement of multiple spin-1 observables. We apply this scheme to an elongated atomic cloud of ^{87}Rb to simultaneously read out three orthogonal spin directions and with that directly access the spatial spin structure. The readout even allows the extraction of quantum correlations which we demonstrate by detecting spin-nematic squeezing without state tomography.

DOI: 10.1103/PhysRevLett.123.063603

Ultracold atomic systems have proven to be a powerful platform for implementing quantum technologies such as quantum simulation [1] and quantum enhanced sensing [2]. For all experimental implementations efficient readout is essential to extract the properties of interest. In fact, advances in readout techniques have paved the way to new discoveries. This includes absorption imaging to observe Bose-Einstein condensation (BEC) [3,4], the quantum gas microscope uncovering spatial correlations in Hubbard models [5] and dispersive methods to observe spin textures in spinor BECs [6].

Here, we show a readout technique to simultaneously access noncommuting spin-1 observables and detect quantum correlations such as coherent spin squeezing. For this we couple the original system to a set of auxiliary states which, combined with unitary transformations, enables the simultaneous readout by measuring all populations in the enlarged Hilbert space [7] [see Fig. 1(a)]. Our readout is especially advantageous in systems with additional spatial degrees of freedom. There, a measurement in a single global basis setting for each experimental realization may not be sufficient to capture all relevant aspects of the quantum state. A prime example is the cluster state, a valuable resource for measurement based quantum computing [8], which features spatial correlations between noncommuting observables [9].

For demonstration, we realize our technique in a spinor Bose-Einstein condensate (BEC) of ^{87}Rb in the $F = 1$ hyperfine manifold. The initially unoccupied $F = 2$ hyperfine states serve as the auxiliary states to which we couple via microwave (MW) pulses [see Fig. 1(b)]. In order to selectively couple the magnetic sublevels in the two manifolds we use two orthogonal radio frequency (rf) coils which generate a rotating magnetic field [14,15]. This exploits the different signs of the corresponding magnetic moments to independently induce spin rotations [see Fig. 1(c)]. Together with MW coupling between the manifolds this gives full control over the measurement basis [14] and in principle allows the simultaneous measurement of seven spin-1 observables out of the eight needed to completely describe a single particle state [16]. Such a readout scheme constitutes a generalized measurement where the formalism of positive operator valued measures (POVM) [17] allows relating the measured populations to the expectation value of spin operators acting on the original system. Compared to sequential imaging schemes [18] or dispersive probing of the different spin directions [6,19] our technique does not introduce backaction from the probing light to the spin state. For ultracold systems this has the advantage that decoherence and heating induced by the probing light are absent.

To demonstrate the possibility to spatially resolve a complex spin structure in a single realization with this readout, we prepare an elongated BEC of ≈40 000 atoms in a dipole trap with trapping frequencies $(\omega_y, \omega_\perp) = 2\pi \times (2.3, 170)$ Hz. All atoms are initialized in the state $(F, m_F) = (1, -1)$ in a magnetic field of $B = 0.884$ G along the z direction. Using spin rotations induced by the rf coils and a magnetic field gradient along the longitudinal direction of the BEC we generate a spin wave involving the three spin directions $\hat{S}_x$, $\hat{S}_y$, and $\hat{S}_z$ [see Supplemental Material (SM) [10] for details]. To read out all three spin directions in a single experimental realization we use the following scheme. We first apply three MW pulses coupling $(1, j) \leftrightarrow (2, j)$ $(j = 0, \pm 1)$ to split the state between the $F = 1$ and $F = 2$ manifold. Selective $\pi/2$ spin rotation in $F = 1$ around the y-axis maps the spin observable $\hat{S}_x$ onto the populations $n_{1,\pm 1}$ and $n_{1,0}$ of $(1, \pm 1)$ and (1,0), respectively. As the $F = 2$ manifold features more magnetic substates than the original system, a $\pi/4$ spin rotation around the x axis in the $F = 2$ manifold allows the extraction of $\hat{S}_y$

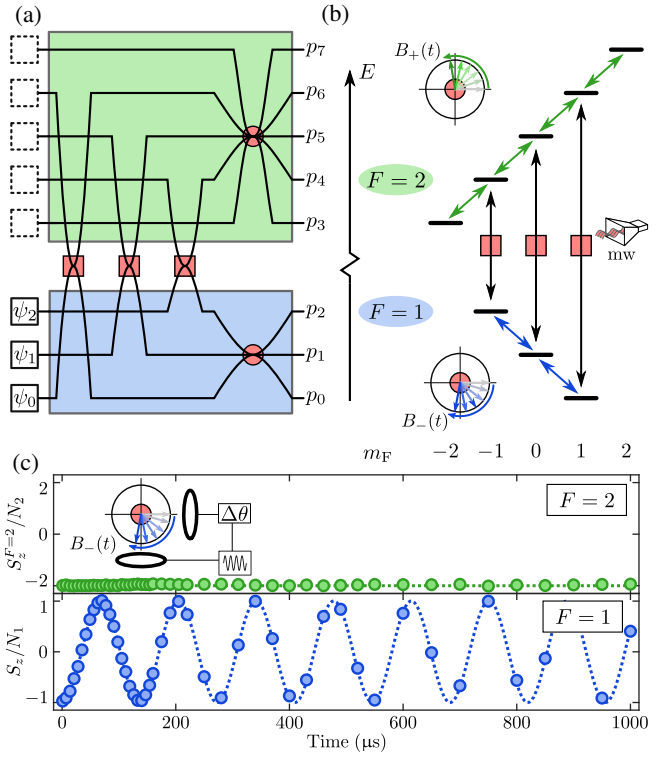

FIG. 1. Schematics of the readout technique. (a) Coupling (red squares) the system (blue) to auxiliary states (green) enlarges the Hilbert space. Applying independent unitaries in both subspaces (red circles) allows choosing the measurement bases individually. From the resulting probabilities $(p_0, \ldots, p_7)$ one infers the corresponding observables of the original system. (b) Level scheme of the electronic ground state of ^{87}Rb in a magnetic field. Coupling the two manifolds with microwave pulses we experimentally realize the extension of the Hilbert space. Rotating magnetic fields selectively couple the magnetic substates in each manifold. (c) Using two rf coils we generate a rotating magnetic field. For a relative phase of $\Delta\theta = -0.7\pi$ we induce spin rotations only in $F = 1$ [10]. For this we measure the z projections S_z and $S_z^{F=2}$ of the spin normalized to the atom numbers N_1 and N_2 detected in the $F = 1$ and $F = 2$ manifold, respectively.

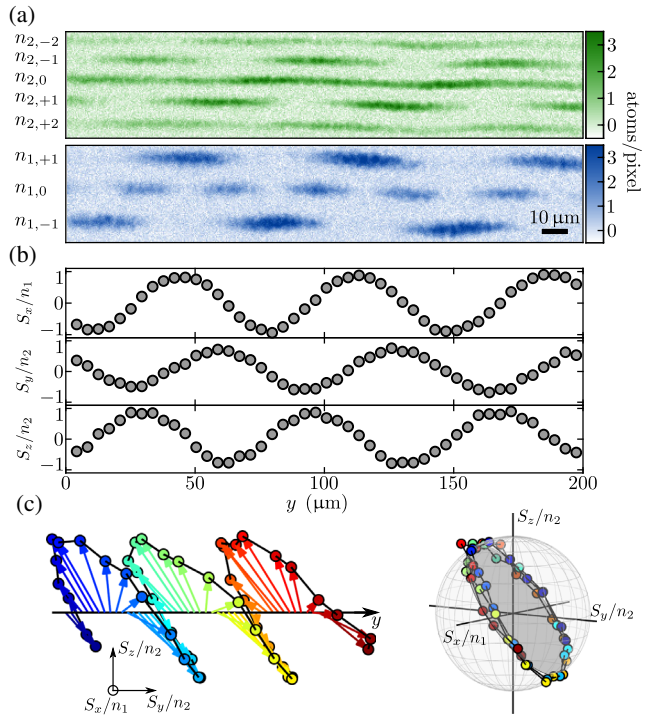

FIG. 2. Spatially resolved readout of three spin components. Using magnetic field gradients and spin rotations we generate a spin wave along the longitudinal direction of an elongated BEC. (a) Populations of the magnetic substates measured via absorption imaging after Stern-Gerlach separation. (b) All three spin directions inferred from the measured populations at each position. The spin observables are normalized to the local atom number $n_F(y)$ in the corresponding hyperfine manifold. (c) Reconstructed spin vector in space and its distribution on a spin sphere.

as well as $\hat{S}_z$. We ensure the phase coherence of all these pulses by active magnetic field stabilization and GPS locking of the rf and MW sources.

With a Stern-Gerlach pulse we spatially separate the different m_F states and use hyperfine selective absorption imaging to measure the population in all magnetic substates with a spatial resolution of ≈1.2 μm as shown in Fig. 2(a). After this sequence the three spin directions are extracted from the measured atom numbers as follows:

$$\begin{aligned} S_x(y) &= \langle \hat{S}_x(y) \rangle_{\delta y} = n_{1,+1}(y) - n_{1,-1}(y), \\ S_y(y) &= \frac{4}{\sqrt{6}}[n_{2,+1}(y) - n_{2,-1}(y)], \\ S_z(y) &= \sqrt{2}[2n_{2,+2}(y) - n_{2,+1}(y), \\ &\quad + n_{2,-1}(y) - 2n_{2,-2}(y)], \end{aligned} \tag{1}$$

where $n_{F,m}(y)$ is the local atom number in the evaluation interval of $\delta y \approx 5$ μm in the state (F, m). Here, $\langle \cdot \rangle_{\delta y}$ denotes the local mean corresponding to an average over ≈700 particles. This measurement yields at every position the three components of the collective spin vector from which we reconstruct the spin wave as shown in Figs. 2(b) and 2(c).

In order to benchmark the capabilities of our readout scheme to extract quantum correlations we prepare an entangled state in our spin-1 system using spin mixing. The resulting spin-nematic squeezed state features correlated fluctuations in two noncommuting observables $\hat{S}_x$ and $\hat{Q}_{yz}$ [20]. Here, $\hat{Q}_{yz}$ is a so-called quadrupole operator which captures an additional degree of freedom inherent to a spin-1 system [10].

In order to constrain the dynamics to the spin degree of freedom we change the trap geometry for this experiment to $(\omega_y, \omega_\perp) = 2\pi \times (40, 170)$ Hz by confining the atomic cloud with an additional crossed dipole beam. We prepare ≈20 000 atoms in the state (1,0) in the spatially symmetric ground state mode. Spin mixing leads to pairwise creation of particles in the states $(1, \pm 1)$ and the energy of (1,0) is tuned such that this process is in resonance with the first

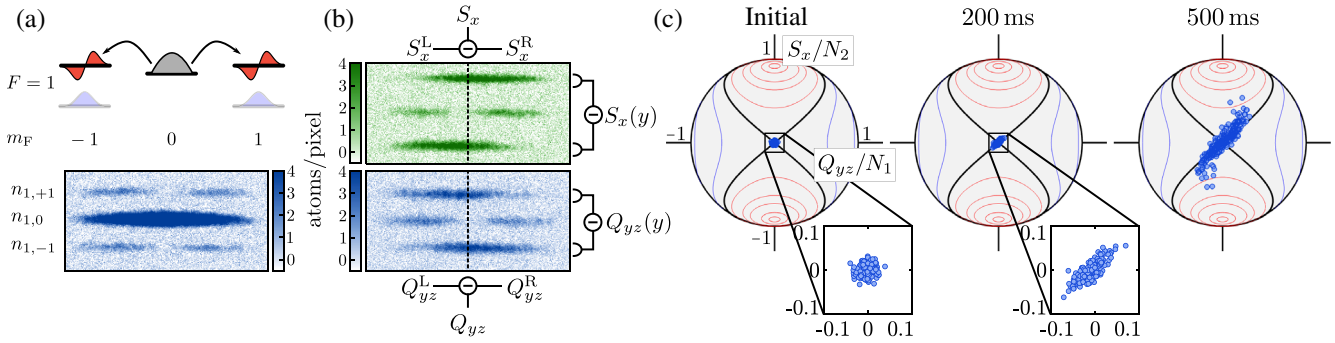

FIG. 3. Efficient detection of spin-mixing dynamics. (a) Using off-resonant MW dressing we tune spin mixing into resonance between the ground mode of (1,0) (gray) and the first excited spatial mode of $(1, \pm 1)$ (red). The lower panel shows an absorption image of the density distributions after 2 s of spin-mixing evolution time where the populations in $(1, \pm 1)$ feature the characteristic double-peak structure. (b) After the readout sequence the observables S_x and Q_{yz} are extracted from the population differences of the states $(2, \pm 2)$ and $(1, \pm 1)$, respectively. Here, the absorption images have been taken after 800 ms of evolution time for better visibility of the mode structure. (c) By plotting the two values for each experimental realization we directly visualize the spin-mixing dynamics in the spin-nematic phase space. The lines correspond to the mean field energy contours of the phase space. For an evolution time of 500 ms a non-Gaussian shape has emerged.

excited spatial mode of the effective external potential for $(1, \pm 1)$ [21]. This mode is spatially antisymmetric which leads to the characteristic double-peak structure of the density in the states $(1, \pm 1)$ [see Fig. 3(a)]. This feature combined with our spatially resolved readout allows the implementation of common mode technical noise rejection as detailed below. To facilitate the absorption imaging we switch off the crossed dipole beam and let the atomic cloud expand in the remaining $\omega_y = 2\pi \times 2.3$ Hz trapping potential for 10 ms.

For a simultaneous readout of both observables, $\hat{S}_x$ and $\hat{Q}_{yz}$, we implement the following scheme. With an rf $\pi/2$ spin rotation around the y direction we map the observable $\hat{S}_x$ on the population difference of the states $(1, \pm 1)$. We then use three MW $\pi/2$ pulses coupling the states $(1, 0/\pm 1)$ with $(2, 0/\pm 2)$ to transfer half of the population to the $F = 2$ manifold. In order to extract $\hat{Q}_{yz}$ we first rotate the state back using an additional rf $\pi/2$ spin rotation around the y axis in $F = 1$. At this stage a spin echo sequence is used to cancel the effect of fluctuations in the magnetic field. We then imprint a phase of $\pi/2$ on the state (1,0) by applying two resonant MW π pulses coupling the states $(1, 0) \leftrightarrow (2, 0)$ with a relative phase of $\pi/2$. An additional rf $\pi/2$ rotation then maps the observable $\hat{Q}_{yz}$ onto the population difference of $(1, \pm 1)$ (see [10] for a graphical illustration of this scheme).

Since the structure of the first excited spatial mode features an opposite sign between left (L) and right (R) half of the atomic cloud [see Fig. 3(b)] we evaluate

$$\begin{aligned} S_x &= S_x^L - S_x^R, \\ Q_{yz} &= Q_{yz}^L - Q_{yz}^R, \end{aligned} \tag{2}$$

with

$$\begin{aligned} S_x^{L/R} &= n_{2,+2}^{L/R} - n_{2,-2}^{L/R}, \\ Q_{yz}^{L/R} &= n_{1,+1}^{L/R} - n_{1,-1}^{L/R}. \end{aligned} \tag{3}$$

This analysis has the additional benefit that it mitigates fluctuations which are homogeneous over the atomic cloud such as technical noise induced by the MW and rf pulses.

For each experimental realization we obtain a point with coordinates S_x and Q_{yz} in the spin-nematic phase space and thus efficiently get an insight into the spin-mixing dynamics. In Fig. 3(c) we show the result for an initial state (1,0), corresponding to the preparation at the unstable fixed point of this phase space, after different evolution times. The state expands along one axis of the separatrix (black line). For longer evolution times $\gtrsim$500 ms the state clearly becomes non-Gaussian which is directly captured with our readout without state reconstruction. Here, we use only $\sim$300 experimental realizations to reveal this feature.

For the short time dynamics one expects to find spin-nematic squeezing below the initial coherent state fluctuations indicating the creation of an entangled many-body state [20]. In Fig. 4(a) we plot the values of S_x/N_2 vs Q_{yz}/N_1 normalized by the total atom numbers N_F measured in the hyperfine manifold $F = 1, 2$ after an evolution time of 100 ms (blue points). The squeezing, i.e., the reduction of fluctuations along one direction at the cost of enhanced fluctuations along the orthogonal direction, is apparent. For a quantitative analysis, we compute the variance $\Delta^2 F(\phi)$ with $F(\phi) = \cos(\phi) Q_{yz} + \sin(\phi) S_x$. Calculating the corresponding atomic shot noise from a multinomial distribution yields $\Delta^2 F(\phi)_{\mathrm{SN}} = \langle \cos^2(\phi) N_1 + \sin^2(\phi) N_2 \rangle$ with which we normalize the variance [see Fig. 4(b)]. Note that for perfect MW $\pi/2$ pulses this term becomes independent of the phase ϕ, while in our experimental realization we observe a small imbalance

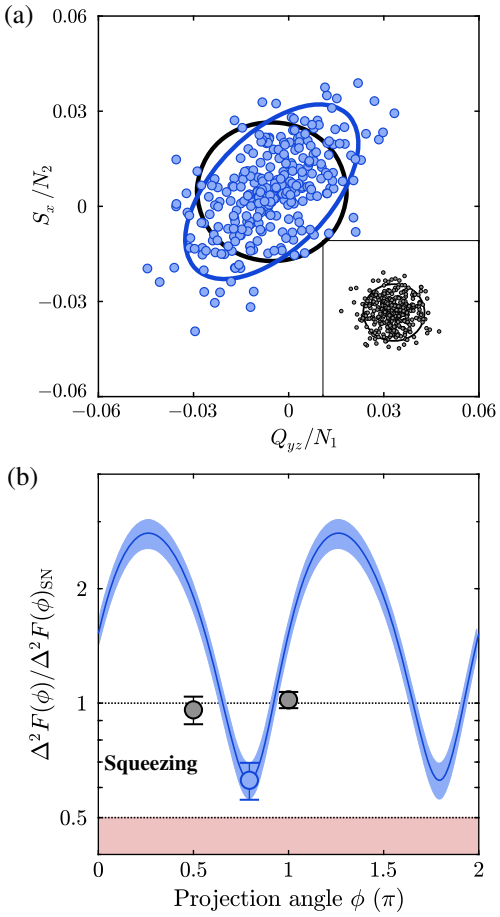

FIG. 4. Detection of spin-nematic squeezing. (a) In each experimental run we obtain a pair of values S_x/N_2 and Q_{yz}/N_1. After 100 ms of evolution time the resulting scatter plot clearly indicates correlated fluctuations between the two observables compared to the initial state (inset). The blue and black line depict the 2 standard deviation (s.d.) interval. (b) For each projection axis parametrized by the angle ϕ we compute the variance. We infer $\Delta^2F(\phi)$ by subtracting imaging noise and normalize to the expected coherent state fluctuations $\Delta^2F(\phi)_{\mathrm{SN}}$ resulting in the blue line and 1 s.d. error band. The prepared state shows reduced fluctuations of 0.62 ± 0.07 (blue point) along the maximally squeezed direction. The red shading indicates the fundamental limit of 0.5 of the readout scheme. The two gray points correspond to the imaging calibration of the $F = 1$ and $F = 2$ manifolds using a coherent spin state. The error bars correspond to the 1 s.d. interval.

corresponding to 0.53π pulses. We infer minimal fluctuations of 0.62 ± 0.07 clearly below the standard quantum limit where independently characterized imaging noise contributions have been subtracted. Without subtraction we find a value of 0.81 ± 0.07. By measuring the fluctuations of a coherent spin state, we independently calibrated our imaging for $F = 2$ and $F = 1$ corresponding to $\phi = 0.5\pi$ and $\phi = \pi$, respectively [10] [gray points in Fig. 4(b)]. After Stern-Gerlach splitting all relevant densities for extracting S_x and Q_{yz} are spatially nonoverlapping since the magnetic moments of $(2, \pm 2)$ are twice as large as the ones of $(1, \pm 1)$. Thus, we extract all populations from a single exposure without the need for hyperfine selective absorption imaging which has the additional benefit of reduced imaging noise.

The noise suppression by nearly a factor of 2 (3 dB) is close to the fundamental limit of our readout method. This limit results from the MW couplings to empty auxiliary states which individually act as beam splitters and thus each introduces additional binomial atom number fluctuations between its output ports. In the case of 50/50 beam splitters, the fluctuations that are extracted from measuring the signal in one port of each beam splitter lead to the estimated variance $\Delta^2F(\phi)$ which is then connected to the variance $\Delta^2F_{\mathrm{in}}(\phi)$ of the input state of the beam splitters as follows:

$$\zeta(\phi) = \frac{\Delta^2F(\phi)}{\Delta^2F(\phi)_{\mathrm{SN}}} = \frac{1}{2}\frac{\Delta^2F_{\mathrm{in}}(\phi)}{N_{\mathrm{tot}}} + \frac{1}{2} \tag{4}$$

with $N_{\mathrm{tot}} = N_1 + N_2$, see SM [10] for details. Therefore, the squeezing measured with this readout cannot submerge the bound of $1/2$ even for vanishing variance $\Delta^2F_{\mathrm{in}}(\phi) = 0$. From the measurement we infer minimal and maximal fluctuations of $\zeta(\phi_{\mathrm{min}}) = 0.62 \pm 0.07$ and $\zeta(\phi_{\mathrm{max}}) = 2.80 \pm 0.25$. Using Eq. (4) we compute $\Delta^2F_{\mathrm{in}}(\phi_{\mathrm{min}})$ $\Delta^2F_{\mathrm{in}}(\phi_{\mathrm{max}}) = (1.1 \pm 0.6)N_{\mathrm{tot}}^2$ consistent with a minimal uncertainty state expected from the dynamics.

In summary, we demonstrate a new technique for the simultaneous readout of multiple spin components of a trapped atomic spinor gas. In situations where a complex valued order parameter arises whose spatial correlations are of interest the simultaneous determination of orthogonal spin components can access these correlations. For example, the easy-plane ferromagnetic phase of a spinor gas is characterized by the order parameter $S_x + iS_y$ [6,22,23]. Furthermore, our readout allows the direct extraction of phase space distributions without state tomography even below the shot noise limit revealing genuine quantum correlations. The ability to extract spatially resolved information about phase space distributions of a state is crucial in situations where *a priori* knowledge about the quantum state is missing. Our method does not build on spatial mode decomposition but is, within the limits of the optical resolution, a truly local measurement. Therefore, in situations of complex multimode dynamics our technique can assess the usefulness of the emerging states for quantum information processing applications such as one-way computation.

We thank Robert Lewis-Swan, Dan Stamper-Kurn, and Daniel Linnemann for discussions and Marcus Huber for pointing out the connection to POVM. This work was supported by the ERC Advanced Grant Horizon 2020 EntangleGen (Project ID 694561) and the DFG

Collaborative Research Center SFB1225 (ISOQUANT), by Deutsche Forschungsgemeinschaft (DFG) under Germany's Excellence Strategy EXC-2181/1—390900948 (the Heidelberg STRUCTURES Excellence Cluster), and the Heidelberg Center for Quantum Dynamics. P. K. acknowledges support from the Studienstiftung des deutschen Volkes.

[1] I. Bloch, J. Dalibard, and S. Nascimbene, Nat. Phys. **8**, 267 (2012).
[2] L. Pezzè, A. Smerzi, M. K. Oberthaler, R. Schmied, and P. Treutlein, Rev. Mod. Phys. **90**, 035005 (2018).
[3] M. H. Anderson, J. R. Ensher, M. R. Matthews, C. E. Wieman, and E. A. Cornell, Science **269**, 198 (1995).
[4] K. B. Davis, M. O. Mewes, M. R. Andrews, N. J. van Druten, D. S. Durfee, D. M. Kurn, and W. Ketterle, Phys. Rev. Lett. **75**, 3969 (1995).
[5] C. Gross and I. Bloch, Science **357**, 995 (2017).
[6] L. Sadler, J. Higbie, S. Leslie, M. Vengalattore, and D. Stamper-Kurn, Nature (London) **443**, 312 (2006).
[7] H. Sosa-Martinez, N. K. Lysne, C. H. Baldwin, A. Kalev, I. H. Deutsch, and P. S. Jessen, Phys. Rev. Lett. **119**, 150401 (2017).
[8] R. Raussendorf, D. E. Browne, and H. J. Briegel, Phys. Rev. A **68**, 022312 (2003).
[9] P. van Loock, C. Weedbrook, and M. Gu, Phys. Rev. A **76**, 032321 (2007).
[10] See Supplemental Material at http://link.aps.org/supplemental/10.1103/PhysRevLett.123.063603 for a definition of the relevant operators, a detailed description of the readout sequences, the calibration of the simultaneous readout of all spin directions, and calibration of the imaging, which includes Refs. [11–13].
[11] I. Carusotto and E. J. Mueller, J. Phys. B **37**, S115 (2004).
[12] W. Muessel, H. Strobel, M. Joos, E. Nicklas, I. Stroescu, J. Tomkovič, D. B. Hume, and M. K. Oberthaler, Appl. Phys. B **113**, 69 (2013).
[13] C. F. Ockeloen, A. F. Tauschinsky, R. J. C. Spreeuw, and S. Whitlock, Phys. Rev. A **82**, 061606(R) (2010).
[14] A. Smith, B. E. Anderson, H. Sosa-Martinez, C. A. Riofrío, I. H. Deutsch, and P. S. Jessen, Phys. Rev. Lett. **111**, 170502 (2013).
[15] H. M. Bharath, M. Boguslawski, M. Barrios, L. Xin, and M. S. Chapman,arXiv:1801.00586.
[16] S. T. Flammia, A. Silberfarb, and C. M. Caves, Found. Phys. **35**, 1985 (2005).
[17] A. Peres, *Quantum Theory: Concepts and Methods* (Kluwer Academic Publishers, New York, 2002), Vol. 57.
[18] G. E. Marti, A. MacRae, R. Olf, S. Lourette, F. Fang, and D. M. Stamper-Kurn, Phys. Rev. Lett. **113**, 155302 (2014).
[19] G. Colangelo, F. M. Ciurana, L. C. Bianchet, R. J. Sewell, and M. W. Mitchell, Nature (London) **543**, 525 (2017).
[20] C. D. Hamley, C. S. Gerving, T. M. Hoang, E. M. Bookjans, and M. S. Chapman, Nat. Phys. **8**, 305 (2012).
[21] M. Scherer, B. Lücke, G. Gebreyesus, O. Topic, F. Deuretzbacher, W. Ertmer, L. Santos, J. J. Arlt, and C. Klempt, Phys. Rev. Lett. **105**, 135302 (2010).
[22] L. A. Williamson and P. B. Blakie, Phys. Rev. Lett. **116**, 025301 (2016).
[23] M. Prüfer, P. Kunkel, H. Strobel, S. Lannig, D. Linnemann, C.-M. Schmied, J. Berges, T. Gasenzer, and M. K. Oberthaler, Nature (London) **563**, 217 (2018).